Large Eddy Simulation of CH$_4$-air and C$_2$H$_4$-air Combustion in a Model Annular Gas Turbine Combustor

N. Zettervall[†], N.A. Worth[‡], M. Mazur[‡], J.R. Dawson[‡] & C. Fureby[†]

[‡]Department of Energy and Process Engineering,
Norwegian University of Science and Technology, N-7491 Trondheim, Norway
[†]Defence Security Systems Technology, The Swedish Defence Research Agency – FOI,
SE 147 25 Tumba, Stockholm, Sweden

Abstract

Combustion instabilities are one of the major challenges in developing and operating propulsion and power generating gas-turbine engines. More specifically, techniques for managing the increasingly stringent emissions regulations and efficiency demands have often given rise to thermo-acoustic instabilities, particularly for annular combustors operating in a lean premixed mode. In this paper, we combine experimental and computational methods to examine unsteady gas turbine combustion in a full annular model gas turbine combustor installed at NTNU, operating both methane- and ethylene-air blends. The experimental data consists of flame images, high-speed OH* chemiluminescence images, as well as pressure and heat-release time-series at discrete locations for the ethylene-air case. The computational set-up consists of the 18 inlet tubes and swirlers, and the full annular combustor placed in a large external domain. The computational model consists of a compressible finite rate chemistry LES model using skeletal methane-air and ethylene-air combustion chemistry. The combustor is simulated in its self-excited state, without external forcing. From the experiments and simulations the methane and ethylene cases are found to behave differently: The ethylene-air flames are much smaller than the methane-air flames, resulting in different interaction between adjacent flames. The LES predictions show good qualitative agreement with the measurements in terms of instantaneous and time-averaged flame structure. Comparing measured and predicted time-series of pressure and heat-release also shows good quantitative agreement with respect to the dynamics and structure for the ethylene-air case. Investigating the predicted combustion dynamics using Proper Orthogonal Decomposition (POD) confirms the importance of the self-excited azimuthal mode on the behavior of the flame: the presence of nodes and anti-nodes of pressure induced fluctuations of the swirler mass-flow, which then, in turn, influence the heat-release. These events occur shifted in time.

1. Introduction and Background

Combustion instabilities, the combination of resonant combustor acoustics and heat-release fluctuations, are one of the major challenges in developing and operating land-, marine- and aircraft gas-turbine engines, [1-3]. More specifically, techniques for managing the increasingly stringent emissions regulations and efficiency demands have often given rise to thermoacoustic instabilities, particularly for lean premixed annular combustors. Thermoacoustic instabilities can be associated with any of the eigenmodes of the combustor, including the longitudinal and transverse (azimuthal and radial) modes. Combustor operating conditions leading to instabilities are almost

impossible to predict *a priori*, and are often only discovered during engine testing, and are thus expensive to cure. To complement full-scale engine tests, [4], we rely on thermo-acoustic solvers, [5], and reduced order models, [6], using flame transfer functions, [7], to identify problematic conditions and engine designs that may promote instabilities. A strategy under development is to use massively parallel finite rate chemistry Large Eddy Simulations (LES) to compute the unsteady dynamics of a complete gas turbine combustor, [8-9].

The origin of the combustion instabilities is that the heat-release fluctuations provide energy to the acoustic field, which results in acoustic pressure and velocity fluctuations traversing the combustor. These fluctuations excite vortical structures and equivalence ratio oscillations that, in turn, give rise to further heat-release fluctuations. A necessary condition for the oscillations to be self-excited is that net energy must be supplied to the acoustic disturbances by the heat-release, which occurs when the phase of the heat-release and pressure oscillations is within ±90°, i.e., the "Rayleigh criterion", [10]. When small amplitude oscillations are self-excited, the amplitude can grow exponentially to develop a limit cycle behavior or resonant frequencies may be excited, potentially leading to combustor or turbine damage and increased emissions. A challenging issue of today is the interest in bio- or low-calorific fuels, having different heat-release and flame properties than conventional fuels. Different thermoacoustic responses may be expected from burning different fuels, and it is thus of importance to improve our knowledge of how the fuel can influence the thermo-acoustics, and which acoustic modes (longitudinal or transverse) that can be expected from operating a given combustor with different fuels.

The primary objective is to improve the understanding of unsteady combustion in annular combustors and how unsteady combustion, with multiple flames, is influenced by the selection of fuel and its heating value. This paper also intends to evaluate the predictive capabilities of finite rate chemistry LES, beyond single combustor configurations previously reported. More specifically we compare and combine results from the experimental investigations of Worth & Dawson, [11-12], operating a model annular multi-burner combustor with methane (CH_4) and ethylene (C_2H_4), with predictions from finite rate chemistry LES, using skeletal reaction mechanisms for the two fuel-air mixtures, [13-14]. The flame dynamics is analyzed using flame- and OH*-chemiluminescence images, computational volume rendering, [15], Proper Orthogonal Decomposition (POD), [16], and pressure and heat-release time-series, and Fast Fourier Transform (FFT) of key experimental and computational quantities.

2. NTNU Model Annular Combustor and Experiments

Figure 1 shows the experimental set-up of the annular combustor which is described in detail in previous investigations, [11-12]. Eighteen (18) premixed flames are spaced around a circle with a diameter of D_a=170 mm, and supplied from a common plenum. Each burner is assembled from a circular tube (L_t=150 mm, D_t=18.9 mm) and a centrally located conical bluff-body (D_{bb}=13.0 mm). A six-vane swirler (vane angle of 60°) is located 10 mm upstream, [12], turning the flow anticlockwise (ACW) when viewed from above (downstream). The 18 flames were located in an annular enclosure formed of inner and outer quartz tubes of D_i=127 mm and D_o=212 mm having different inner and outer lengths of L_i=130 and L_o=300 mm respectively.

Three Alicat mass flow controllers with ranges of 0-33 l/s for air and 0-8 l/s for fuel were used to regulate the reactant flow rates. Each controller has a measurement accuracy of 0.8% of the reading with ±0.2% of the full scale. A bulk velocity of v_o=18 m/s results in a Reynolds (Re) number of 15,600 based on D_{bb} and the reactant viscosity. Ethylene (C_2H_4) and methane (CH_4) flames were investigated, at an equivalence ratio ϕ=0.85, [11-12].

To characterize the response, the pressure was measured at three equally spaced locations around the annulus. At each location, a pair of Kulite XCS-093 pressure transducers with a sensitivity of $4.28 \cdot 10^3$ mV/Pa, range of 0.35 atm, and accuracy of ±0.15% full scale were positioned along the inlet pipes and mounted flush with the inside walls. Measurements were acquired at 30 kHz with sample lengths of 4.30 s. To study the flame structure high-speed OH* chemiluminescence images of the annular combustor were obtained from the side using a Photron SA1.1 high-speed CMOS camera coupled with a LaVision IRO high-speed two-stage intensifier, fitted with
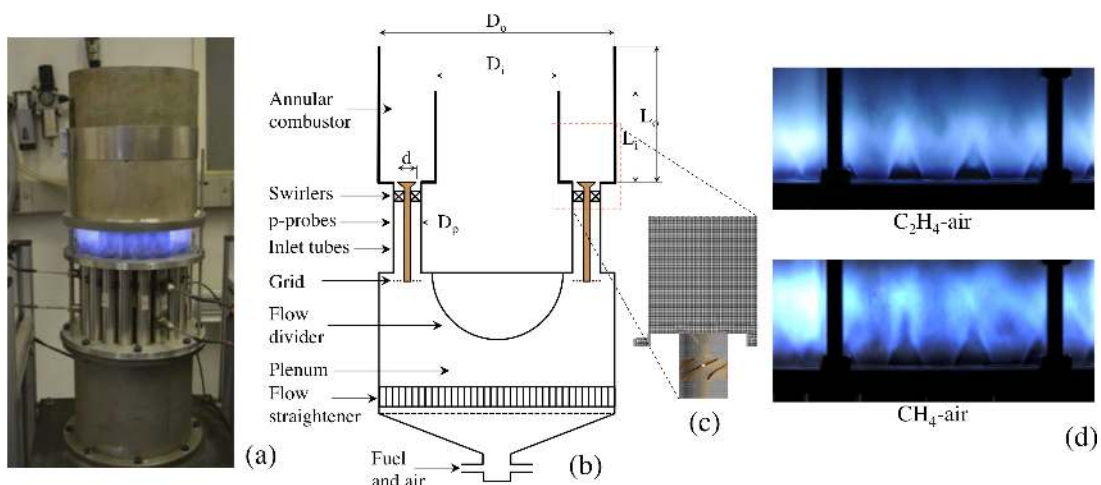
Fig. 1. Photograph, (a) experimental set-up diagram (b), mesh detail (c) and C_2H_4-air and CH_4-air flame images (d) of the Worth & Dawson model annular combustor, [11-12].

a Cerco 2178 UV 100F/2.8 lens and a narrow band UV filter (305-315 nm). A total of 2000 im-

ages were captured at a frame rate of 10,000 fps at a pixel resolution of 495×748, giving a spatial resolution of approximately 10 pixels/mm.

3. LES Models, Numerical Methods and Computational Set-Up

The LES model is based on implicitly-filtered transport equations for mass, momentum, energy and species mass-fractions, [17], together with thermal and caloric equations-of-state and constitutive equations. The thermal and caloric equations-of-state are obtained under the presumption of a mixture of thermally perfect gases using tabulated formation enthalpies and specific heats. The constitutive equations are those of a linear viscous mixture with Fickian diffusion and Fourier heat conduction. The viscosity is calculated using Sutherland's law, whereas the thermal conductivity and species diffusivities are computed from the viscosity utilizing constant Prandtl and species Schmidt numbers, respectively, [18]. The unfiltered reaction rates in the filtered species mass-fraction equations results from Guldberg-Waage law of mass-action, involving the summation over all reactions, with reaction rates obtained from Arrhenius rate laws, [19].

The unresolved transport terms, or the subgrid stress tensor and flux vectors, in the filtered transport equations are closed by the mixed model, [20]. The filtered reaction rates are modeled using the Partially Stirred Reactor (PaSR) model, [21], which is a multi-scale model based on the observation, [22], that combustion often takes place in dispersed fine-structure regions surrounded by low intensity regions. The filtered reaction rates are estimated as a weighted average of the fine-structure and surrounding reaction rates using the reacting volume fraction, γ^*. This model has been extensively used in combustion LES, and is validated for laboratory flames, [23-24], afterburners, [25], gas turbine combustors, [26], and ram/scramjet combustors, [27].

The LES-PaSR model equations are solved using a semi-implicit finite volume code based on the OpenFOAM C++ library, [28]. High-order monotonicity preserving reconstruction of the convective fluxes and central differencing of the inner derivatives in the diffusive fluxes, [29], are combined with Crank-Nicholson time-integration to provide a second order accurate scheme. The code uses a compressible Pressure-based Implicit Splitting of Operators (PISO), [30], technique to manage the pressure-velocity-density coupling. The chemical source terms in the species transport equations are evaluated using an operator-splitting approach using a Rosenbrock solver, [31]. Stability is enforced using compact stencils and a Courant number<0.5.

The computational set-up includes the inlet tubes, swirlers, annular combustor, and a large external volume. Both single sector and full annular geometries, with 18 burners, are considered. At the inlets, fuel and air mass-flows are provided, and at the outlet, a wave-transmissive bound-

ary condition is specified, [32], given an ambient pressure of 1.0 atm. The effect of the upstream plenum was deemed negligible by performing an additional simulation using a plenum boundary condition, [33]. In the inlet tubes, swirlers and combustor, a no-slip LES wall-model is used for the velocity together with zero Neumann conditions for the species mass-fractions. The inlet tubes and swirlers have adiabatic wall-temperature boundary conditions whereas the combustor wall-temperature is estimated to be 1000 K. Hex-dominant grids with ~4 and ~72 million cells, respectively, for the single sector and full annular combustor are employed. Topologically identical but finer grids, with ~8 and ~144 million cells, were used to examine the grid sensitivity using the LES Index of Quality, [34], approach, revealing that 85% and 91%, respectively, of the kinetic energy was resolved, rendering both grids appropriate for LES. In addition, the y^+ values are 10 to 60 as required by the LES wall model, [35]. Simulations are first performed (for both the CH_4-air and C_2H_4-air cases) in the single sector configuration, after which these results are mapped and rotated onto the annular configuration, after which the simulation are restarted and statistics gathered.

4. CH_4-air and C_2H_4-air Chemical Kinetics

The CH_4-air and C_2H_4-air combustion mechanisms are modeled using the pathway centric skeletal reaction mechanisms, Z42, [13], and Z66, [14], respectively. The mechanisms are sufficiently detailed to describe the flame properties, but small enough (42 and 66 reactions, respectively) to be used in finite-rate chemistry LES. The two skeletal mechanisms share the same general structure that can be described by the three successive steps: (i) fuel-decomposition (including H abstraction), (ii) fuel-radical chemistry, and (iii) H-C-O chemistry as described in [13-14]. The first step is fuel specific, the second step is generic for small radicals and fuel-specific for large radicals, and the third step is generic. For C_2H_4 the Aramco 2.0 mechanism, [36], was used as reference in combination with experimental data, [14], whereas for CH_4 the GRI 3.0 mechanism, [37], was used as reference in combination with experimental data, [38-40].

Figures 2a, 2b and 2c compare predictions and experimental data for s_u and T_{flame} at 1 atm and 300 K, and τ_{ign} at 1 atm, respectively. Concerning s_u, both Z42 and Z66 are in good agreement with the experimental data and the predictions from the GRI3.0 and Aramco mechanisms, respectively. For T_{flame}, Z42 matches the temperature prediction from GRI3.0 well but shows a small overprediction at highly fuel rich conditions. Z66 agrees well with the Aramco mechanism but with small deviations at around stoichiometric conditions. Both the Z66 and Aramco mechanisms predict slightly lower temperatures compared to the experimental data. Regarding τ_{ign}, Z42

6

and Z66 overpredict τ_{ign} at low T compared to the reference mechanisms. However, as T increases both mechanisms improve their predictions of τ_{ign}.
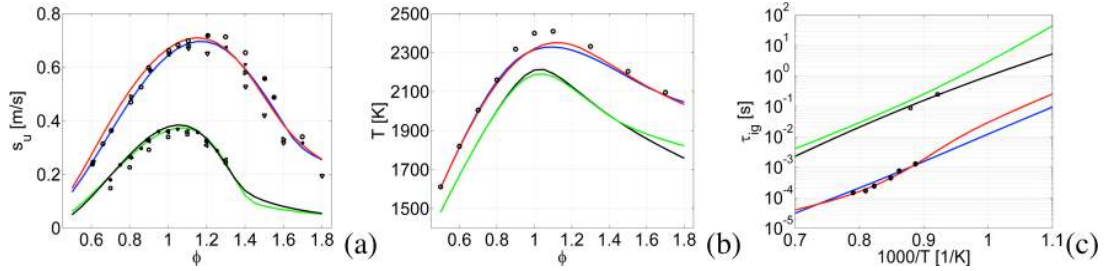
Fig. 2. (a) Laminar flame speeds, s_u and (b) flame temperatures, T_{flame} at 1 atm and 300 K, and (c) ignition delay times at $\phi=1.0$ and p=1.1 atm. Legend: experimental data for s_u for CH_4, [38-40], and C_2H_4, [14], for T for C_2H_4, [14], and for τ_{ign} for CH_4, [39], and for C_2H_4, [14]. Mechanism predictions from (—) Z42, [13], (—) GRI3.0, [37], (—) (Z66), [14], and (—) Aramco, [36].

5. Results and Discussion

Figure 1d presents flame images from C_2H_4-air and CH_4-air combustion, from which it is evident that the C_2H_4-flames are virtually detached and smaller than the CH_4-flames, which show strong flame interactions. Experiments, [11], suggest that different fuels, C_2H_4 and CH_4, may result in fuel-specific combustion dynamics. The LES results in Fig. 3 initially confirm this observation as illustrated by the volumetrically rendered heat-release, Q. Fig. 3 also includes contour maps of the axial velocity, v_x, (left), temperature, T, (right) and pressure, p, (top), as well as combined volumetric renderings of C_2H_3/CH_3, CH_2O and HCO for an annotated burner and flame. The volumetric renderings of Q from the LES show that the structures of the C_2H_4-flames are quite regular, whereas the structures of the CH_4-flames are more irregular, having a wide and topologically complex overlap region with a more filamented structure. This is due to the higher s_u and lower τ_{ign} of C_2H_4 compared to CH_4, Fig 2, resulting in faster ignition, and smaller, more compact C_2H_4 flames, located closer to the burners. The wider CH_4 flames, having lower extinction strain rates, σ_{ext}, than the C_2H_4 flames, extend further into the combustor and interact more actively with the turbulence, resulting in increased flame area and delayed exothermicity compared to the C_2H_4 flames The increased flame area for the CH_4 flames also makes these flames more susceptible to acoustic perturbations. Furthermore, from the LES we estimate the integral length scales, ℓ_i, and velocity fluctuations, v', from which we compute the Dahmköhler (Da) and Karlowitz (Ka) numbers to be Da≈9.3 and 2.3, and Ka≈4.7 and 18.9, respectively, for the C_2H_4- and CH_4-cases. Hence, both cases reside in the lower part of the thin reaction sheets regime, with the CH_4-case, showing the most intense turbulence-chemistry interactions.

The v_x distribution is similar for both cases, involving funnel-shaped, high-speed, fuel-rich,

regions discharging from the inlet tubes, via the swirlers, into the combustor, a Central Recirculation Zone (CRZ) downstream of each bluff-body, and an Outer Recirculation Zone (ORZ) enclosing each of the flames at its base. The CRZ's and the ORZ's are unsteady, and the ORZ's are connected, forming a composite flow structure dominated by an unsteady vortex. Further downstream, v_x increases due to the volumetric expansion from the exothermicity. The larger (and weaker) CH_4-flames cause the fuel jets to penetrate further into the combustor, changing the size and shape of the CRZ, influencing also the volumetric expansion.

The T distribution consists of funnel-shaped low-temperature regions discharging from the burners. These regions vary significantly in size and shape between the C_2H_4- and CH_4-cases and between burners due to the differences in combustion chemistry (s_u, τ_{ign}, T_{flame} and σ_{ext}), turbulence-chemistry interactions, flame area, exothermicity and volumetric expansion. Further downstream, the T distribution is quite homogeneous, except in the boundary layers, and the difference in flame temperature (2212 K and 2067 K) between the cases.

The flame structure is noticeably fuel-dependent as evident by the species distributions in the inserts of Fig. 3. For the C_2H_4-case, individual flames are evident, consisting of several thin wrinkled layers of species, consistent with the reaction path diagram, [14]. For the CH_4-case, individual flames can no longer be observed since the CH_4-flames are higher and wider, and are overlapping the neighboring flames. These differences can be traced back to the differences in s_u, τ_{ign}, T_{flame} and σ_{ext}, resulting in more pronounced turbulence-chemistry interactions and increased flame area for the CH_4-flames compared to the C_2H_4-flames. Moreover, the difference in pressure also influences the flame structures. The higher Ka number of the CH_4-case supports the observations of a more turbulent and wrinkled flame structure.
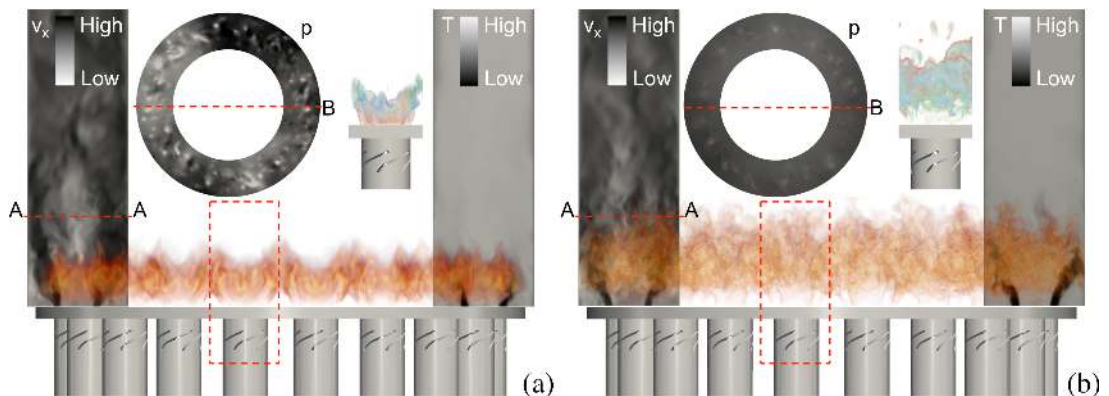
Fig. 3. Instantaneous LES predictions from the (a) C_2H_4- and (b) CH_4-air cases. Shown are contour maps of the axial velocity, v_x, (left side of section A-A), temperature, T, (right side of section A-A), pressure, p, (top view of section B-B), heat-release, Q, (volumetric rendering), and species, CH/C_2H_3 (green), CH_2O (blue) and HCO (red) renderings from the annotated burner.

8

At a first glance, the p distribution seems to be governed by azimuthal modes for the C_2H_4-case and longitudinal modes for the CH_4-cases. By examining LES animations we find that both flames display irregular motions and flame wrinkling at multiple scales, during a rotating or helical motion. Moreover, the CH_4-flames oscillate mainly in the longitudinal direction whereas the C_2H_4-flames appear more prone to azimuthal oscillations. The animations can however not define any distinct modes as these are coupled, and hence a different technique must be used to analyze the modal structures and the interactions.

Figure 4 compare instantaneous and time-averaged side-views of OH* chemiluminescence images from the experiments with LES-based volumetric renderings of Q for the C_2H_4- and CH_4-cases. The experimental C_2H_4-flames are ~30 mm high with reactions occurring only in the inner shear-layer, and interactions between neighboring flames occurring ~1.25 D_{bb} downstream of the dump-plane, with a large number of flame-elements stabilized in the region between neighboring flames. The flame-brushes appears to bend slightly outwards as the reactants enter the combustor and hence remain relatively straight. The predicted C_2H_4-flames are ~27 mm high with reactions occurring in both the inner and outer shear-layers. The predicted flame-brushes also bend slightly outwards as the reactants enter the combustor, but gradually turn towards the axial direction of the combustor, resulting in small overlap regions between flames. The predicted C_2H_4-flames are less wrinkled, with fewer and less fragmented flame-elements than the experimental C_2H_4-flames. The experimental CH_4-flames are ~45 mm high, with reactions occurring intermittently in the inner and outer shear-layers, but further downstream compared with the C_2H_4-flames. The flame-brushes are initially straight, but as adjacent flames converge they seems to bend away from each other, resulting in a larger distance to where the strongest interaction occur (~1.50 D_{bb}). The predicted CH_4-flames are ~45 mm high with reactions in both the inner and outer shear-layers. The
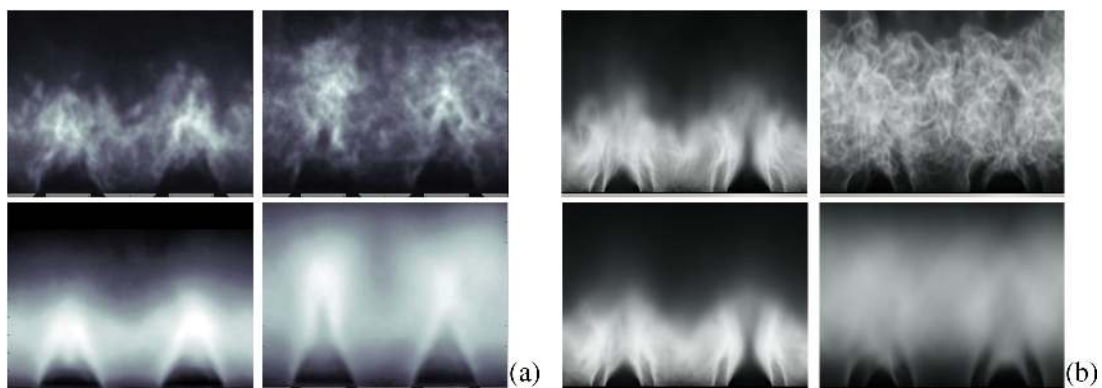

Fig. 4. Side-views of (a) instantaneous (top) and time-averaged (bottom) experimental OH* images from the C_2H_4-case (left) and the CH_4-case (right), and (b) instantaneous (top) and time-averaged (bottom) Q distributions from the LES of the C_2H_4-case (left) and the CH_4-case (right).

flame-brushes are topologically convoluted, and appear more turbulent, wrinkled and fragmented, and with more flame-elements, than the laboratory CH_4-flames. Both the measured and predicted, instantaneous and time-averaged, C_2H_4- and CH_4-flames are qualitatively similar, and the trends observed in the experiments and LES are the same.

Figure 5 compares time-series of normalized pressure- and heat-release fluctuations, p'/p_0 and Q'/Q_0, from experiments and LES. For the C_2H_4-case we notice that the LES results are less regular than the experimental data, for which p'/p_0 reveals distinct sinusoidal signals at 1720 Hz. Based on D_a and the speed-of-sound, c, at $\phi=0.85$, the first azimuthal mode have a frequency of $c/(\pi D_a) \approx 1728$ Hz, and this together with the fact that the pressure signals are 120° apart implies that this is indeed an azimuthal mode, [11-12]. The p'/p_0 signals from the LES is more irregular; an FFT-analysis of the time-series in figure 5a shows that it is dominated by a 1715 Hz signal, with additional contributions at 907 and 3345 Hz. For the Q'/Q_0 signals in figure 5b we find these to be dominated by a ~1720 Hz mode in the experimental case and a ~1685 Hz mode in the LES case. For the CH_4-case, LES suggest different dynamics compared to the C_2H_4-case; The p'/p_0 signals are dominated by two frequencies at 934 and 1708 Hz. Based on D_a and c, the frequency of the first azimuthal mode is $c/(\pi D_a) \approx 1686$ Hz, which correlates well with the predicted 1708 Hz mode, suggesting that this is an azimuthal mode. The 934 Hz signal is thus inferred to be the first (quarter-wave) longitudinal mode, $c/(4L)$, with $L_i<L<L_o$. The Q'/Q_0 signal is less regular, revealing peaks completely uncorrelated with the p'/p_0 signals. These results suggests that the heat-release from the two fuels interacts differently with the flows, resulting in dissimilar pressure perturbations, which in turn couples back to the flow and heat-release.
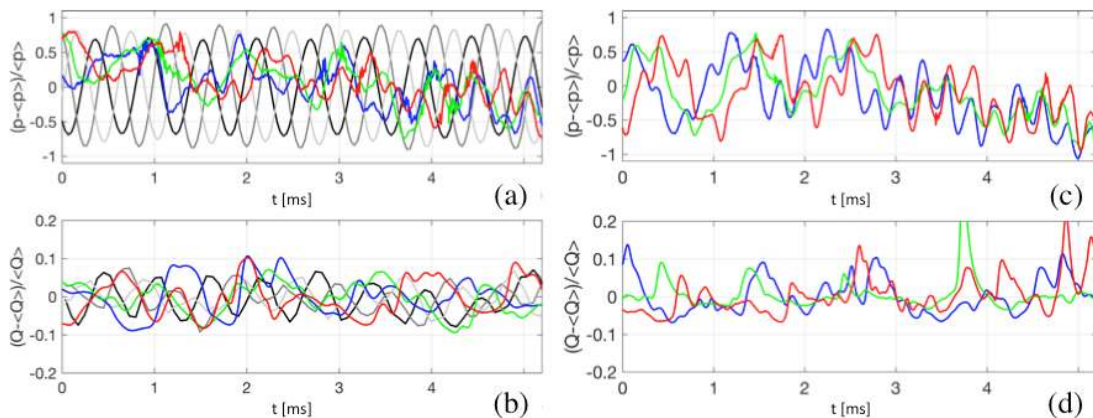

Fig. 5. Time-series (at three locations 120° apart) of pressure fluctuations, p'/p_0, (a) and (c), and heat-release fluctuations, Q'/Q_0, (b) and (d), from experiments (black, dark gray and light gray) and LES (red, blue and green) from the C_2H_4-case (a) and (b) and the CH_4-case (c) and (d).

The combustion dynamics are further analyzed with POD, [17], by which a field, $\phi=\phi(\mathbf{x},t)$,

can be expressed using basis functions, $\Psi_i^\phi(\mathbf{x})$, and coefficients, $\omega_i^\phi(t)$, derived from the LES so that $\phi(\mathbf{x},t)=\Sigma_{i=0}^N \omega_i^\phi(t)\Psi_i^\phi(\mathbf{x})$. Here, the method of snapshots, [41], is used to compute $\omega_i^\phi(t)$ and $\Psi_i^\phi(\mathbf{x})$. The lowest POD modes sampled over 40 ms, Ψ_1^p, Ψ_2^p, Ψ_3^p, Ψ_0^Q, Ψ_1^Q and Ψ_0^v of p, Q and $\mathbf{v}$ are presented in Figs. 6a and 6b for the C_2H_4 and CH_4 cases, respectively, and Figs. 6c and 6d present the corresponding POD coefficients, ω_i^ϕ. Here, 100 snapshots have been used, resulting in that the four lowest order POD modes contain ~60% of the respective variable energy.

The POD analysis shows that the C_2H_4-case, featuring small flames and large central recirculation regions in Ψ_0^Q and Ψ_0^v, respectively, is dominated by two co-rotating azimuthal modes, Ψ_1^p and Ψ_2^p, and a longitudinal mode, Ψ_3^p. The CH_4-case, featuring large flames and small central recirculation regions in Ψ_0^Q and Ψ_0^v, respectively, is dominated by two counter-rotating azimuthal modes, Ψ_1^p and Ψ_2^p, and a longitudinal mode, Ψ_3^p. The co-rotating lowest-order modes in the C_2H_4-case interact, making the resulting azimuthal mode, $\Psi_1^p+\Psi_2^p$, the governing mode. As in the experiments, [11], this mode rotates mainly in the anti-clock-wise direction at ~1725 Hz as corroborated by Fig. 5. The lowest-order counter-rotating modes in the CH_4-case negate each other, making Ψ_3^p, and the resulting azimuthal mode, $\Psi_1^p-\Psi_2^p$, the dominating ones at 924 and 1698 Hz, respectively. The first heat-release mode, Ψ_1^Q, dominates the lower part of the combustor, revealing large differences depending on the case in terms of size and shape, with Ψ_1^Q being more fragmented in the region of high pressure fluctuations. These modal structures occur shifted in time as described by $\omega_1(t)$ in Fig. 6b. The delay between velocity and heat-release may then be extracted to assess the response of the burner to a velocity fluctuation.
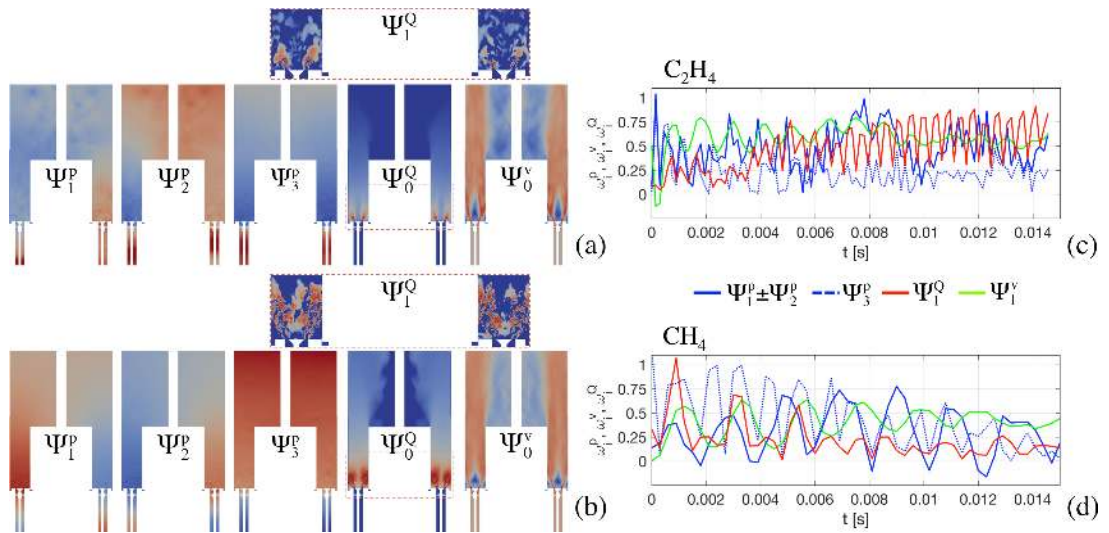
Fig. 6. POD modes for the (a) C_2H_4- and (b) CH_4-cases together with time-series of the POD coefficients for the lowest POD modes for the (c) C_2H_4- and (d) CH_4-cases.

6. Summary and Concluding Remarks

This paper describes a combined experimental and computational investigation of a full annular academic gas turbine combustor configuration installed at NTNU, operating both methane- and ethylene-air blends. The experimental data include flame images, OH* chemiluminescence images, and pressure and heat-release time-series at sensors, 120° apart, [11-12], for the ethylene-air case. The computational set-up consists of the full annular combustor, including inlet tubes and swirlers, in a large external domain. The LES model consists of a compressible finite-rate chemistry LES model with skeletal methane-air and ethylene-air chemistry.

From experiments and LES' the CH_4- and C_2H_4-air cases are found to behave quite differently: The C_2H_4-air flames are considerably smaller than the CH_4-air flames due to the difference in s_u, resulting in different interactions between adjacent flames. For the C_2H_4-air case, LES and experimental results present good qualitative and quantitative agreement with respect to instantaneous and time-averaged flame structures, and pressure and heat-release time-series. Based on POD the combustion dynamics is found to be governed by two co-rotating azimuthal modes, resulting in an anti-clockwise azimuthal mode at ~1725 Hz in conjunction with an associated heat-release mode. This behavior is corroborated by the experimental results. The combustion dynamics of the CH_4-case is composed of two counter-rotating modes, essentially negating each other, resulting in a weak azimuthal mode at 1698 Hz, and a dominating longitudinal mode at 924 Hz. This difference in modal behavior is also corroborated by preliminary experimental results. The main difference between the cases is the difference at which heat is released and how the heat-release interacts with the pressure- and velocity-fields. This study demonstrates that LES can predict complex flame-acoustics phenomena also in real combustors.

References

[1]   H.C Mongia, T.J Held, G.C. Hsiao, R.P Pandalai, in: T.C. Lieuwen, V. Yang (Eds.), Combustion Instabilities in Gas Turbine Engines, AIAA, Washington D.C., 2005, p 43.

[2]   K. Smith, J. Blust, in: T.C. Lieuwen, V. Yang (Eds.), Combustion Instabilities in Gas Turbine Engines, AIAA, Washington D.C., 2005, p 29.

[3]   W. Krebs, S. Bethke, J. Lepers, P. Flohr, B. Prade, in: T.C. Lieuwen, V. Yang (Eds.), Combustion Instabilities in Gas Turbine Engines, AIAA, Washington D.C., 2005, p 89.

[4] D. Kroniger, P. Vinnemeier, C. Rudolf, M. Wirsum M., GT2014-26736 (2014).

[5] F. Nicoud, L. Benoit, C. Sensiau, T. Poinsot, AAAI 45 (2007) 426-441.

[6] A.P. Dowling, J. Sound Vib. 180 (1995) 557-581.

[7] N. Noiray, D. Durox, T. Schuller, S. Candel S., J. Fluid Mech. 615 (2008) 139-167.

[8] P Wolf, G. Staffelbach, L.Y.M. Gicquel, J. Muller, T. Poinsot, Comb. Flame, 159 (2012) 3398-3414.

[9] N. Zettervall, E. Fedina, K. Nordin Bates, E. Heimdal Nilsson, C. Fureby, AIAA 2015-4020 (2015).

[10] J. O'Connor, V. Acharya, T. Lieuwen, Prog. Energy Combust. Sci. 49 (2015) p 1-39.

[11] N.A. Worth, J.R. Dawson, Combust. Flame 160 (2013) 2476-2489.

[12] N.A. Worth, J.R. Dawson, Proc. Combust. Inst. 34 (2013) 3127-3134.

[13] A. Larsson, N. Zettervall, T. Hurtig, E.J.K. Nilsson, A. Ehn, P. Petersson, M. Aldén, J. Larfeldt, C. Fureby, Energy Fuels 31 (2017) 1904-1926.

[14] N. Zettervall, C. Fureby, E.J.K. Nilsson, "Small Skeletal Kinetic Reaction Mechanism for Ethylene-Air Combustion", Accepted for publication in Energy & Fuels (2017).

[15] A. Watt, M. Watt, Advanced Animation and Rendering Techniques: Theory and Practice, Addison-Wesley, Reading, Massachusetts, USA (1992).

[16] G. Berkooz, P. Holmes, J.L. Lumley, Annu. Rev. Fluid Mech. 25 (1993) 539-575.

[17] T. Echekki, E. Mastorakos, Turbulent Combustion: Concepts, Governing Equations and Modeling Strategies in Turbulent Combustion Modeling: Advances, New Trends and Perspectives, Springer, Netherlands, 2011.

[18] E. Giacomazzi, F.P. Picchia, N. Arciacono, On the Distribution of Lewis and Schmidt Numbers in Turbulent Flames, 30th Italian Meeting on Combustion, Ischia, Italy (2007).

[19] S. Menon, C. Fureby, Computational Combustion in: R. Blockley, W. Shyy (Eds.), Encyclopedia of Aerospace Engineering, John Wiley & Sons, 2010.

[20] R. Bensow, C. Fureby, J. Turb. 8(54) (2007) 1-17.

[21] V Sabelnikov C. Fureby Combust. Flame 160 (2013) 83-96.

[22] M. Tanahashi, M. Fujimura, T. Miyauchi, Proc. Combust. Inst. 28 (2000) 529-535.

[23] K-J. Nogenmyr, C. Fureby, X.-S. Bai, P. Petersson, M. Linné, Comb. Flame 156 (2009) 25-36.

[24] E. Fedina, C. Fureby, J. Turb. 12(24) (2011) 1-20.

[25] N. Zettervall, K. Nordin-Bates, E. Heimdal-Nilsson, C. Fureby, Combust. Flame 179 (2015) 1-22.

[26] E. Fedina, C. Fureby, G. Bulat, W. Maier, Flow, Turb. and Combust., 99 (2017) 385-409.

[27] K. Nordin-Bates, C. Fureby, S. Karl, K. Hannemann K, Proc. Combust. Inst. 35 (2017) 2893-2900.

[28] H.G. Weller, G. Tabor, H. Jasak, C. Fureby, Comp. in Physics 12 (1997) 620-631.

[29] D. Drikakis, C. Fureby, F.F. Grinstein, M. Liefendahl, in; Implicit Large Eddy Simulation: Computing Turbulent Fluid Dynamics, F.F. Grinstein, L. Margolin, B. Rider (Eds.), Cambridge University Press (2007) p 94.

[30] N.W. Bressloff, Int. J. Num. Methods in Fluids, 36 (2001) 497-518.

[31] E. Hairer, G. Wanner, Solving Ordinary Differential Equations, II: Stiff and Differential-Algebraic Problems, 2nd Ed., Springer Verlag Berlin Heidelberg (1996).

[32] T.J. Poinsot, S.K. Lele, J. Comp. Phys., 101 (1992) 104-129.

[33] Bainbridge W.D.Q.; 2013, "The Numerical Simulation of Oscillations in Gas Turbine Combustion Chambers", PhD Thesis, Cambridge University Department of Engineering, Cambridge, UK.

[34] I. Celik, Z.N. Cehreli, I. Yavuz, ASME, J. Fluids Engineering, 127 (2005) 949-958.

[35] Fureby C.; 2017, "High Fidelity Numerical Simulations of Ship and Submarine Hydrodynamics", VII Int. Conf. on Comp. Methods in Marine Engng. MARINE 2017, Eds. Visonneau M., Queutey P. & Le Touzé D.

[36] W.K. Metcalfe, S.M. Burke, S.S. Ahmed, H.J. Curran, Int. J. Chem. Kin., 45 (2013) 638-675.

[37] http://www.me.berkeley.edu/gri_mech/

[38] M. Goswami, S.C.R Derks K. Coumans W.J. Slikker, M.H. de Andrade Oliveira, R.J.M. Bastiaans, C.C.M. Luijten, L.P.H. de Goey, A.A. Konnov A.A., Combust. Flame 160 (2013) 1627-1635.

[39] O. Park, P.S. Veloo, N. Lui, F.N. Egolfopoulos, Proc. Combust. Inst. 33 (2011) 887-894.

[40] W. Lowry, J. de Vries, M. Krejci, E. Peterson, Z. Serinyel, W. Metcalfe, H.J. Curran, G. Bourque, J. Eng, Gas Turbines Power 133 (2011) 091501.

[41] L. Sirovich, Quarterly Appl. Math. XLV (1987) 561-571.

Figure Captions

Fig. 1. Photograph, (a) experimental set-up diagram (b), mesh detail (c) and C_2H_4-air and CH_4-air flame images (d) of the Worth & Dawson model annular combustor, [11-12].

Fig. 2. (a) Laminar flame speeds, s_u and (b) flame temperatures, T_{flame} at 1 atm and 300 K, and (c) ignition delay times at ϕ=1.0 and p=1.1 atm. Legend: experimental data for s_u for CH_4, [38-40], and C_2H_4, [14], for T for C_2H_4, [14], and for τ_{ign} for CH_4, [39], and for C_2H_4, [14]. Mechanism predictions from (—) Z42, [13], (—) GRI3.0, [37], (—) (Z66), [14], and (—) Aramco, [36].

Fig. 3. Instantaneous LES predictions from the (a) C_2H_4- and (b) CH_4-air cases. Shown are contour maps of the axial velocity, v_x, (left side of section A-A), temperature, T, (right side of section A-A), pressure, p, (top view of section B-B), heat-release, Q, (volumetric rendering), and species, CH_3/C_2H_3 (green), CH_2O (blue) and HCO (red) renderings from the annotated burner.

Fig. 4. Side-views of (a) instantaneous (top) and time-averaged (bottom) experimental OH* images from the C_2H_4-case (left) and the CH_4-case (right), and (b) instantaneous (top) and time-averaged (bottom) Q distributions from the LES of the C_2H_4-case (left) and the CH_4-case (right).

Fig. 5. Time-series (at three locations 120° apart) of pressure fluctuations, p'/p_0, (a) and (c), and heat-release fluctuations, Q'/Q_0, (b) and (d), from experiments (black, dark gray and light gray) and LES (red, blue and green) from the C_2H_4-case (a) and (b) and the CH_4-case (c) and (d).

Fig. 6. POD modes for the (a) C_2H_4- and (b) CH_4-cases together with time-series of the POD coefficients for the lowest POD modes for the (c) C_2H_4- and (d) CH_4-cases.